Effects of Vibrational Nonequilibrium on Hypersonic Shock-Wave/Laminar Boundary-Layer Interactions

Jiaao Hao[a], Chih-Yung Wen[a,*]

[a] Department of Mechanical Engineering, The Hong Kong Polytechnic University, Kowloon, Hong Kong

Abstract

Recent numerical simulations of hypersonic double-cone and hollow-cylinder flare experiments have incorrectly predicted the sizes of separation regions, even at total enthalpies as low as 5.44 and 5.07 MJ/kg. This study investigates the effects of vibrational nonequilibrium to explain these discrepancies. According to an assessment of various flow models under post-shock conditions in comparison with state-specific simulations, the predictions obtained by treating the vibrational modes of molecular nitrogen and oxygen as a single mode, a strategy adopted routinely by the aerospace computational fluid dynamics community, are in close agreement with the state-specific results in terms of post-shock temperature and density profiles, whereas separation of the vibrational modes and assumption of calorically perfect gases would lead to evident errors. The double-cone flow is found to be sensitive to different flow models. In contrast, their effects on hollow-cylinder flare flow are insignificant. Given that the most representative flow model still underestimates the sizes of the separation regions for double cone flow and overestimates those for hollow-cylinder flare flow, it is concluded that inaccurate modeling of vibrational nonequilibrium may not be responsible for the discrepancies observed at the lowest total enthalpies. Suggestions for further study are also presented.

Keywords: hypersonic; thermochemical nonequilibrium; shock-wave/boundary-layer interaction

1 Introduction

Shock-wave/boundary-layer interaction (SWBLI) is frequently encountered in hypersonic flight and can lead to high aerothermodynamic loads. Accurate predictions

---

*Corresponding author
Email address: cywen@polyu.edu.hk

of SWBLI are of vital importance to the design of hypersonic vehicles.

Extensive experiments [1–6] using canonical configurations have been conducted to evaluate the ability of modern computational fluid dynamics (CFD) tools to predict hypersonic laminar interactions in thermochemical nonequilibrium states. This study investigates the double-cone and hollow-cylinder flare experiments performed in 2013 by Holden et al. [7] in the LENS XX expansion tunnel at Calspan—University of Buffalo Research Center. In these experimental studies, surface pressure and heat flux were measured in air at total enthalpies between 5.44 and 21.77 MJ/kg for a 25–55 deg double-cone configuration and from 5.07 to 21.85 MJ/kg for a 30 deg hollow-cylinder flare. The numerical results from various studies [8–14] have been compared with the experimental data. It was found that the CFD simulations tended to underestimate the sizes of the separation regions for the double cone and overestimate the sizes of the separation bubbles for the hollow-cylinder flare. The causes for these discrepancies remain poorly understood. It is commonly suspected that inaccurate modeling of air chemistry might be a major reason [7]. However, given that very few chemical reactions would occur at the lowest total enthalpies, it may be inferred that the discrepancies observed under these conditions have a different cause. Specifically, this study investigated the effects of vibrational nonequilibrium on the double-cone and hollow-cylinder flare flows at total enthalpies of 5.44 and 5.07 MJ/kg to explain the discrepancies.

The paper is organized as follows: Different flow models are discussed in Section 2, including a mixture of perfect gases with vibrational nonequilibrium, a mixture of perfect gases with vibrational nonequilibrium of separate modes, and a mixture of calorically perfect gases. Section 3 presents an assessment of these models under post-shock conditions using state-specific results as a reference. In Section 4, the distributions of surface pressure and heat flux predicted by different flow models are compared with the experimental data.

2 Flow models

Based on different treatments of vibrational nonequilibrium, three flow models are considered in this work. In these models, the molecules' rotational energy mode is

assumed to be fully excited and in equilibrium with the translational mode of heavy particles in terms of a translational–rotational temperature, T_{tr}. The processes of electronic excitation and ionization are neglected.

2.1 Model I: mixture of perfect gases with vibrational nonequilibrium

In model I, the flow is assumed to be in thermal nonequilibrium according to Park's two-temperature model [15], in which the vibrational levels of molecules are described by harmonic oscillators and populated in Boltzmann distributions in terms of a single vibrational temperature, T_v. The finite-rate air chemistry is considered to be frozen. Because only molecular nitrogen and oxygen are present in the experimental freestreams, the fluid medium is described as a two-species (N_2, O_2) mixture with the mass fractions remaining unchanged throughout the flowfields. The corresponding governing equations comprise the conservation equations of species mass, mixture momentum, total energy, and mixture vibrational energy. Here, only the equation of mixture vibrational energy is presented as

$$\frac{\partial \rho e_v}{\partial t} + \frac{\partial \rho e_v u_j}{\partial x_j} = -\frac{\partial q_{v,j}}{\partial x_j} - \frac{\partial}{\partial x_j}\left(\sum_{s=\text{mol.}} J_{s,j} e_{v,s}\right) + \omega_v , \tag{1}$$

where the index mol. denotes molecular species; ρ is the density of the mixture; e_v and $e_{v,s}$ are the specific vibrational energies of the mixture and species s, respectively; $\boldsymbol{q}_v$ is the vibrational heat flux vector; $\boldsymbol{J}_s$ is the mass diffusion flux vector of species s; and ω_v is the vibrational energy source term, given by

$$\omega_v = \omega_{t-v} + \omega_{v-d} . \tag{2}$$

The term ω_{t-v} is the energy transfer between the translational and vibrational modes, which is modeled using the Landau–Teller model [16] and the Millikan–White expression [17] with Park's high-temperature correction [18]. The term ω_{v-d} is the added or removed vibrational energy induced by recombination and dissociation, which here is equal to zero due to the frozen chemistry.

Model I is one of the routine options widely used in the aerospace CFD community to represent the vibrational nonequilibrium processes.

2.2 Model II: mixture of perfect gases with vibrational nonequilibrium of separate modes

In model II, the flow is also assumed to be a two-species mixture without chemical reactions. Instead of modeling the mixture vibrational energy, the vibrational modes of molecular nitrogen and oxygen are treated separately with the corresponding conservation equations given by

$$\frac{\partial \rho_s e_{v,s}}{\partial t} + \frac{\partial \rho_s e_{v,s} u_j}{\partial x_j} = -\frac{\partial q_{v,s,j}}{\partial x_j} - \frac{\partial J_{s,j} e_{v,s}}{\partial x_j} + \omega_{v,s}, \tag{3}$$

where $s = N_2$ and O_2. Because no chemistry is considered in this model, the vibrational energy source term, $\omega_{v,s}$, simply contains two parts: $\omega_{t-v,s}$ and $\omega_{v-v,s}$. The $\omega_{t-v,s}$ term is modeled in the same manner as model I, whereas $\omega_{v-v,s}$, which represents the vibrational energy transfer between different molecules, is expressed in the following form [19]:

$$\omega_{v-v,s} = \sum_{r \neq s} N_{Av} \sigma_{sr} \rho_s \rho_r \sqrt{\frac{8 k_B T_{tr}}{\pi \mu_{sr}}} \left(P_{sr} \frac{e_{v,r}}{M_s} - P_{rs} \frac{e_{v,s}}{M_r} \right), \tag{4}$$

where N_{Av} is the Avogadro constant, σ_{sr} is the collision cross section, k_B is the Boltzmann constant, μ_{sr} is the reduced mass, M_s is the molecular mass of species s, and P_{sr} is the probability of vibration–vibration exchange between species s and r. For N_2–O_2 interactions, the probability is taken from Park and Lee [20].

Model II can be regarded as an upgrade of model I, but its accuracy relies on the modeling of $\omega_{v-v,s}$.

2.3 Model III: mixture of calorically perfect gases

To further examine the effects of vibrational nonequilibrium, model III assumes that the flow is described by a two-species mixture of calorically perfect gases. Here, no vibrational excitation is considered, thus the vibrational energy equation can be removed. The corresponding governing equations are similar to the conventional Navier–Stokes equations for a calorically perfect gas except that the conservation of mass is established for each species.

3 Assessment of different vibrational nonequilibrium models

Because the only difference between models I, II, and III lies in the treatment of

vibrational nonequilibrium, it is of interest to investigate which model provides the most accurate description of vibrational excitation before the numerical results and experimental data are compared for hypersonic SWBLI. In this section, these models are therefore assessed under post-shock conditions, using the results obtained from the state-specific simulation as a reference.

3.1 State-specific simulation

The vibrational elementary processes considered in the state-specific simulation contain the vibration–vibration–translation (V–V–T) bound–bound transitions induced by N_2–N_2, N_2–O_2, and O_2–O_2 collisions. The resulting master equation for the number density of N_2 at vibrational level i can be expressed as

$$\frac{\partial\left[N_2(i)\right]}{\partial t} = \left\{\frac{\partial\left[N_2(i)\right]}{\partial t}\right\}_{V-V-T}^{N_2-N_2} + \left\{\frac{\partial\left[N_2(i)\right]}{\partial t}\right\}_{V-V-T}^{N_2-O_2}, \tag{5}$$

$$\left\{\frac{\partial\left[N_2(i)\right]}{\partial t}\right\}_{V-V-T}^{N_2-N_2} \\ = \sum_m\sum_n\sum_j\left\{k_{V-V-T}^{N_2-N_2}(m,n\to i,j)\left[N_2(m)\right]\left[N_2(n)\right] - k_{V-V-T}^{N_2-N_2}(i,j\to m,n)\left[N_2(i)\right]\left[N_2(j)\right]\right\} \tag{6}$$

$$\left\{\frac{\partial\left[N_2(i)\right]}{\partial t}\right\}_{V-V-T}^{N_2-O_2} \\ = \sum_m\sum_n\sum_j\left\{k_{V-V-T}^{N_2-O_2}(m,n\to i,j)\left[N_2(m)\right]\left[O_2(n)\right] - k_{V-V-T}^{N_2-O_2}(i,j\to m,n)\left[N_2(i)\right]\left[O_2(j)\right]\right\} \tag{7}$$

where [A] represents the number density of species A, $k_{V-V-T}(i,j\to m,n)$ is the rate coefficient of V–V–T transitions (with superscripts representing the interaction type), and i, j, m, and n represent the vibrational quantum numbers of the colliding molecules. The master equation for O_2 can be established in a similar manner.

The 61 and 46 vibrational levels given by Lopez and Lino da Silva [21] are considered here for molecular nitrogen and oxygen, respectively, in the ground electronic state. The rate coefficients of V–V–T transitions are calculated based on forced harmonic oscillator theory, whose accuracy was validated by comparison with the results determined by semiclassical trajectory calculations for single-quantum transitions [22,23] by Lino da Silva et al. [24]. Generally, the forced harmonic oscillator model may provide an alternative solution for V–V–T transition rate

coefficients when the quasi-classical trajectory data are unavailable.

In the shock reference frame, the master equations are directly coupled to the one-dimensional compressible flow equations to trace the spatial variation of each vibrational level of N_2 and O_2 behind a normal shock. To reduce the computational cost, the multi-quantum V–V–T transitions with jumps larger than 5 are assumed to be negligible according to the heat bath calculations of Andrienko et al. [25] and the post-shock simulations of Hao et al. [26]. The initial condition is derived from the Rankine–Hugoniot relations assuming a frozen chemical composition and a vibrational mode. The governing equations are then integrated using the explicit fourth-order Runge–Kutta scheme.

3.2 Post-shock flows

The vibrational nonequilibrium flow behind a normal shock wave under the double-cone flow condition (see Table 1) is simulated using the state-specific method. Models I, II, and III are also used to predict the post-shock flow with the governing equations described in Section 2 reduced to the respective one-dimensional compressible flow equations.

Figure 1 compares the post-shock profiles of temperatures predicted by various models as a function of the distance from the shock. Note that only the translational–rotational temperatures are shown in the figure for model III and the state-specific method. The different models have similar translational–rotational temperatures immediately behind the shock. However, the distinct behaviors of these temperatures can be observed as the flows develop downstream of the shock. For models I and II, the translational–rotational temperature declines gradually due to the excitation of the vibrational mode until a state of equilibrium is achieved. In contrast, the post-shock temperature remains constant for model III. It can be seen that the predictions of model I have the best agreement with the state-specific result. The separation of the vibrational mode in model II leads to much slower vibrational relaxation, which could be attributed to a modeling error of the vibration–vibration energy exchange between N_2 and O_2. It is clear that treating the flow as a mixture of calorically perfect gases in model III results in substantial overestimation of the translational–rotational

temperature.

Figure 2 shows the post-shock density profiles predicted by various models. Because the post-shock pressure is insensitive to the thermodynamics, the density behind the shock is roughly inversely proportional to the translational–rotational temperature. Consequently, model I predicts a greater density in the relaxation zone than model II, but their equilibrium values are identical. Model III produces a constant post-shock density that is much lower than the vibrational nonequilibrium results. Again, the profile obtained from model I has the closest agreement with the state-specific result. Note that a small gap exists between the equilibrium value from the state-specific simulation and that predicted by models I and II, which is caused by differences in the evaluation of the vibrational energy. Once the harmonic oscillator model is replaced by the vibrational levels of N_2 and O_2 used in the state-specific method, the difference is eliminated.

4 Computational details

The numerical simulations in this investigation are performed with a multi-block parallel finite-volume CFD code called PHAROS [27,28]. The inviscid terms are evaluated using the modified Steger–Warming scheme [29] and extended to higher orders with monotone upstream-centered schemes for conservation laws (MUSCL) reconstruction [30] with the van Leer slope limiter [31]. The viscous fluxes are calculated using a second-order central difference. A line relaxation method [32] is used for time marching.

The viscous stresses are modeled with the assumption of a Newtonian fluid and Stokes' hypothesis. Heat fluxes are calculated according to Fourier's law for all energy modes. The species mass diffusion fluxes are modeled using the modified Fick's law to ensure that the sum of the diffusion fluxes is zero [33]. The transport properties of the gas mixture are calculated using Gupta's mixing rule [34] with the collision integral data given by Wright et al. [35].

The geometries of the double-cone and hollow-cylinder flare configurations are illustrated in Ref. [7]. The two flow conditions simulated in this study are listed in Table 1, where M is the Mach number; V_∞, T_∞, and ρ_∞ are the freestream velocity,

temperature, and density, respectively; h_0 is the specific total enthalpy; and Re_∞ is the unit Reynolds number. Due to the relatively low Reynolds numbers, the flows are assumed to be laminar. The test gas was air in a thermochemical equilibrium state with mass fractions of 0.765 and 0.235 for N_2 and O_2, respectively [7]. In addition, the model surfaces are assumed to be non-catalytic and fixed at a constant temperature of 300 K.

Table 1. Freestream conditions for the double-cone and hollow-cylinder flare simulations [7].

Configuration	M	V_∞ (km/s)	T_∞ (K)	ρ_∞ (g/m^3)	h_0 (MJ/kg)	Re_∞ (m^{-1})
Double cone	12.2	3.246	175	0.499	5.44	1.4×10^5
Hollow-cylinder flare	11.3	3.123	189	0.634	5.07	1.5×10^5

It is well known that the level of numerical dissipation is important to the prediction of hypersonic SWBLI, and careful selection of the numerical schemes and computational grid resolution is therefore required. According to Druguet et al. [36], the modified Steger–Warming scheme with the van Leer limiter should be qualified for the simulations in this study. In addition, computational meshes with 1024 and 512 nodes in the axial and radial directions, respectively, would be sufficient to ensure grid convergence. Hao et al. [14] provided a complete description of the grid independence study for the double-cone configuration. In both cases, the grids are constructed with the origin of the coordinate system located at the head of the model and the horizontal axis along the axis of revolution. The normal spacing at the surfaces is set to 1×10^{-7} m to ensure that the grid Reynolds number has an order of magnitude of one. Approximately 150 characteristic flow times are simulated to ensure time convergence.

5 Results

5.1 Effects of chemical reactions

In this section, the effects of chemical reactions on double-cone and

hollow-cylinder flare flows are examined by comparing the distributions of the surface quantities predicted with model I with and without chemical reactions. When chemical nonequilibrium effects are involved, a five-species (N_2, O_2, NO, N, O) finite-rate air chemistry model [18] is used. To consider the vibration–dissociation coupling effects, a controlling temperature defined by the geometric average of T_{tr} and T_v with half power is used to evaluate the nonequilibrium dissociation rate coefficients. In addition, ω_{v-d} is modeled using the nonpreferential model [37].

Figure 3 shows the predicted profiles of surface pressure and heat flux along the surface of the double-cone configuration as a function of the axial distance. Note that the large increase in pressure and the sinking of the heat flux near $x = 7$ cm correspond to the separation of the boundary layer on the first cone and that the pressure and heat flux peaks are caused by flow reattachment and shock impingement on the second cone, respectively. The profiles are nearly identical in both cases, indicating that the effects of air chemistry are insignificant under the present condition. In fact, the temperature increase in the interaction region is relatively low, hence very few chemical reactions occur. Quantitatively, the maximum mass fractions of atomic N and O are less than 6.85×10^{-7} and 3.20×10^{-4}, respectively. Given that the interaction induced by the hollow-cylinder flare configuration is much weaker than that generated by the double cone, overlapped distributions of surface pressure and heat flux are obtained, as shown in Fig. 4.

5.2 Comparison with experiments

Figure 5 compares the distributions of surface pressure and heat flux predicted by different flow models for the double-cone configuration and shows the experimental data. Treating the vibrational mode separately in model II slightly increases the size of the separation bubble, whereas the exclusion of vibrational excitation in model III leads to substantial enlargement of the separation region in comparison with the results predicted by model I. The locations of the peak pressure and heat flux also move downstream when model III is used, but there is no change in the peak values. It seems that all three models tend to underestimate the size of the separation region when compared with the experimental pressure data. In contrast, the experimental

heat flux data are enclosed by the numerical results. The locations of the sudden changes in numerical surface pressure and heat flux on the first cone indicating flow separation are identical, but they clearly differ when deduced from experimental distributions. More experimental data are therefore required to exclude the measurement error.

To further demonstrate the difference between the results of models I and III, the contours of the density gradient magnitude predicted by the two models are examined in Fig. 6. The observed shock structures are similar in both cases and resemble Edney's type V shock interaction [38], featured by regular reflection of the transmitted shock near the impingement point and a thin supersonic jet bounded by slip lines. Although the attached shock is largely unaffected by different models, the detached shock is much closer to the surface when the process of vibrational excitation is considered. This phenomenon could be attributed to the vibrational excitation absorbing the translational energy of the flow and reducing the post-shock translational temperature (see Fig. 7), leading to a greater post-shock density and thus a shorter shock standoff distance.

Figure 8 compares the distributions of the surface pressure and heat flux predicted by different models with the experimental data for the hollow-cylinder flare configuration. The three models predict overlapped distributions, which implies that the effects of vibrational nonequilibrium are weak. Compared with the experimental data, the numerical results overpredict the size of the separation region and fail to correctly capture the peak pressure and heat flux.

6 Conclusions

In this paper, three different flow models, including a mixture of perfect gases with vibrational nonequilibrium (model I), a mixture of perfect gases with vibrational nonequilibrium of separate modes (model II), and a mixture of calorically perfect gases (model III), are considered to examine the effects of vibrational nonequilibrium on double-cone and hollow-cylinder flare flows at total enthalpies of 5.44 and 5.07 MJ/kg, corresponding to the cases with the lowest enthalpy in a recently conducted series of experiments.

These models are compared with state-specific results under post-shock conditions. Model I makes the most accurate predictions in terms of post-shock temperature and density profiles. The separation of the vibrational modes in model II leads to much slower vibrational relaxation due to the inaccurate modeling of the vibration–vibration energy exchange, whereas model III significantly overestimates the post-shock translational–rotational temperature and underestimates the post-shock density.

The distributions of surface pressure and heat flux predicted by different models are compared with the experimental data. Accurate modeling of vibrational excitation is essential to predict the double-cone flow, whereas the hollow-cylinder flare flow is insensitive to the vibrational nonequilibrium models. Although the results of model I could closely follow the state-specific profiles under post-shock conditions, the CFD simulations performed using model I still tend to underestimate the size of the separation on the double cone and overestimate the size of the separation bubble on the hollow-cylinder flare. Therefore, inaccurate modeling of vibrational nonequilibrium might not be responsible for the discrepancies observed under the present conditions. It is suggested that more experimental data are required to exclude the measurement error, and simulations could be performed to investigate the effects of transport properties models, slip boundary conditions, and flow nonuniformity in the test section. Further examinations of the modeling of air chemistry and vibration–dissociation coupling would be meaningful only after good agreement with the experiment achieved at relatively low total enthalpies.

Acknowledgements

References

[1] M. S. Holden, T. P. Wadhams, Code validation study of laminar shock/boundary layer and shock/shock interactions in hypersonic flow, part A: experimental measurements, AIAA 2001–1031A, 2001.

[2] J. K. Harvey, M. S. Holden, T. P. Wadhams, Code validation study of laminar shock/boundary layer and shock/shock interactions in hypersonic flow, part B: comparison with Navier–Stokes and DSMC solutions, AIAA 2001–1031B, 2001.

[3] M. S. Holden, T. P. Wadhams, M. Maclean, Experimental studies in the LENS supersonic and hypersonic tunnels for hypervelocity vehicle performance and code validation, AIAA 2008–2505, 2008.

[4] I. Nompelis, G. V. Candler, M. MacLean, T. P. Wadhams, M. S. Holden, Numerical investigation of double-cone flow experiments with high-enthalpy effects, AIAA 2010–1283, 2010.

[5] A. Swantek, J. Austin, Heat transfer on a double wedge geometry in hypervelocity air and nitrogen flows, AIAA 2012–0284, 2012.

[6] M. S. Holden, T. P. Wadhams, M. Maclean, A. Dufrene, Experimental research and analysis in supersonic and hypervelocity flows in the LENS shock tunnels and expansion tunnel, AIAA 2015–3660, 2015.

[7] M. S. Holden, M. Maclean, T. P. Wadhams, A. Dufrene, Measurements of real gas effects on regions of laminar shock wave/boundary layer interaction in hypervelocity flows for "blind" code validation studies, AIAA 2013–2837, 2013.

[8] I. Nompelis, G. V. Candler, US3D predictions of double-cone and hollow cylinder-flare flows at high enthalpy, AIAA 2014–3366, 2014.

[9] G. V. Candler, Next-generation CFD for hypersonic and aerothermal flows, AIAA 2015–3048, 2015.

[10] M. R. Youssefi, D. Knight, Assessment of CFD capability for hypersonic shock wave boundary layer interactions, part II, AIAA 2016–0350, 2016.

[11] N. Kianvashrad, D. Knight, Simulation of hypersonic shock-wave–laminar-boundary-layer interaction on hollow cylinder flare, AIAA J., 55(1) (2017) 322–326.

[12] N. Kianvashrad, D. Knight, Simulation of hypersonic shock wave laminar boundary layer interaction on hollow cylinder flare, part II, AIAA 2017–3975, 2016.

[13] K. Vogiatzis, E. Josyula, P. Vedula, Double-cone flows in nonequilibrium:

comparison of CFD with experimental data, AIAA 2017–0664, 2017.

[14] J. Hao, J. Wang, C. Lee, Numerical simulation of high-enthalpy double-cone flows, AIAA J., 55(7) (2017) 2471–2475.

[15] C. Park, Two-temperature interpretation of dissociation rate data for N_2 and O_2, AIAA 1988–0458, 1988.

[16] W. G. Vincenti, C. H. Kruger, Introduction to physical gas dynamics, Krieger, Malabar, 1965.

[17] R. C. Millikan, D. R. White, Systematics of vibrational relaxation, J. Chemical Physics, 39(12) (1963) 3209–3213.

[18] C. Park, Nonequilibrium hypersonic aerothermodynamics, Wiley, New York, 1990.

[19] G. V. Candler, The computation of weakly ionized hypersonic flows in thermo-chemical nonequilibrium, Stanford University, 1988.

[20] C. Park, S.-H. Lee, Validation of multi-temperature nozzle flow code noznt, AIAA 1993–2862, 1993.

[21] B. Lopez, M. Lino da Silva, Non-Boltzmann analysis of hypersonic air re-entry flows, AIAA 2014–2547, 2014.

[22] G. D. Billing, E. R. Fisher, VV and VT rate coefficients in N_2 by a quantum-classical model, Chemical Physics, 43(3) (1979) 395–401.

[23] G. D. Billing, R. E. Kolesnick, Vibrational relaxation of oxygen. State to state rate constants, Chemical Physics Letters, 200(4) (1992) 382–386.

[24] M. Lino da Silva, V. Guerra, J. Loureiro, State-resolved dissociation rates for extremely nonequilibrium atmospheric entries, J. Thermophysics and Heat Transfer, 21(1) (2007) 40–49.

[25] D. A. Andrienko, K. Neitzel, I. D. Boyd, Vibrational relaxation and dissociation in O_2–O mixtures, AIAA 2016–4021, 2016.

[26] J. Hao, J. Wang, C. Lee, State-specific simulation of oxygen vibrational excitation and dissociation behind a normal shock, Chemical Physics Letters 681 (2017) 69–74.

[27] J. Hao, J. Wang, C. Lee, Numerical study of hypersonic flows over reentry

configurations with different chemical nonequilibrium models, Acta Astronautica, 126 (2016) 1–10.

[28] J. Hao, J. Wang, C. Lee, Development of a Navier–Stokes code for hypersonic nonequilibrium simulations, AIAA 2017–2164, 2017.

[29] R. W. MacCormack, Numerical computation of compressible and viscous flow, AIAA, Reston, 2014.

[30] B. van Leer, Towards the ultimate conservative difference scheme, J. Computational Physics, 32(1) (1979) 101–136.

[31] E. F. Toro, Riemann solvers and numerical methods for fluid dynamics a practical introduction, Springer, Berlin, 1997.

[32] M. J. Wright, G. V. Candler, D. Bose, Data-parallel line relaxation method for the Navier–Stokes equations, AIAA J., 36(9) (1998) 1603–1609.

[33] K. Sutton, P. A. Gnoffo, Multi-component diffusion with application to computational aerothermodynamics, AIAA 1998–2575, 1998.

[34] R. N. Gupta, J. M. Yos, R. A. Thompson, K. P. Lee, A review of reaction and thermodynamic and transport properties for an 11-species air model for chemical and thermal nonequilibrium calculations to 30 000 K, NASA RP-1232, 1990.

[35] M. J. Wright, D. Bose, G. E. Palmer, E. Levin, Recommended collision integrals for transport property computations, part 1: air species, AIAA J., 43(12) (2005) 2558–2564.

[36] M.-C. Druguet, G. V. Candler, I. Nompelis, Effect of numerics on Navier–Stokes computations of hypersonic double-cone flows, AIAA J., 43(3) (2005) 616–623.

[37] P. A. Gnoffo, R. N. Gupta, J. L. Shinn, Conservation equations and physical models for hypersonic air flows in thermal and chemical nonequilibrium, NASA TP-2867, 1989.

[38] B. E. Edney, Effects of shock impingement on the heat transfer around blunt bodies, AIAA J., 6(1) (1968) 15–21.
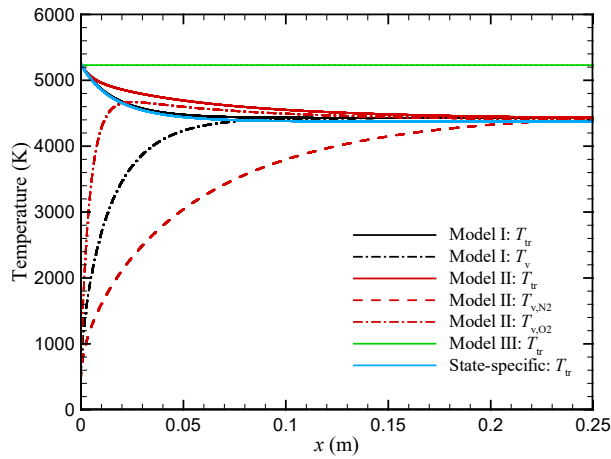
Fig. 1. Post-shock temperature profiles predicted by different models.
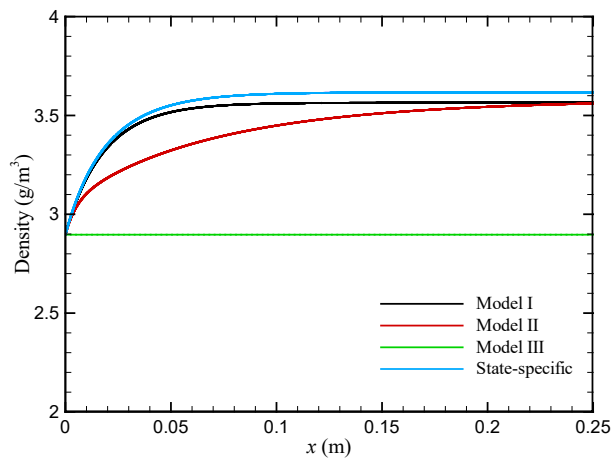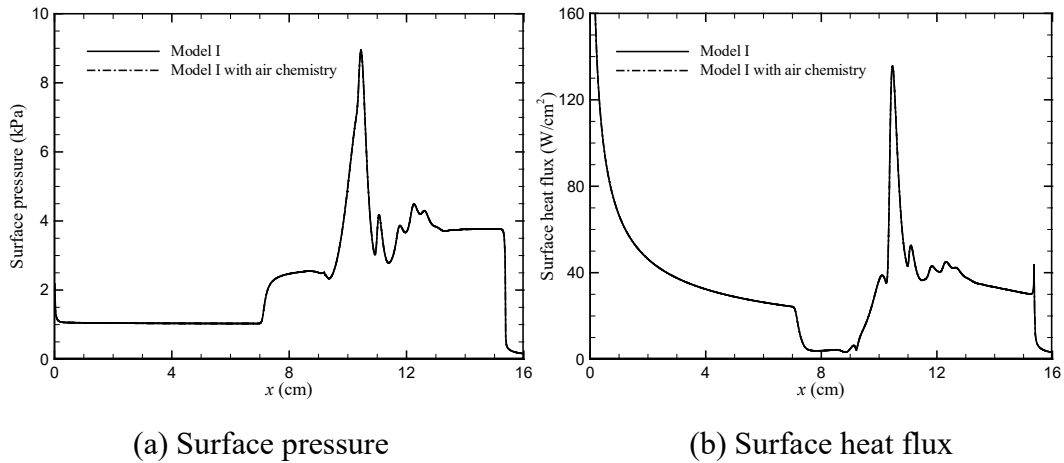

Fig. 2. Post-shock density profiles predicted by different models.

(a) Surface pressure   (b) Surface heat flux

Fig. 3. Distributions of surface pressure and heat flux predicted by models I with
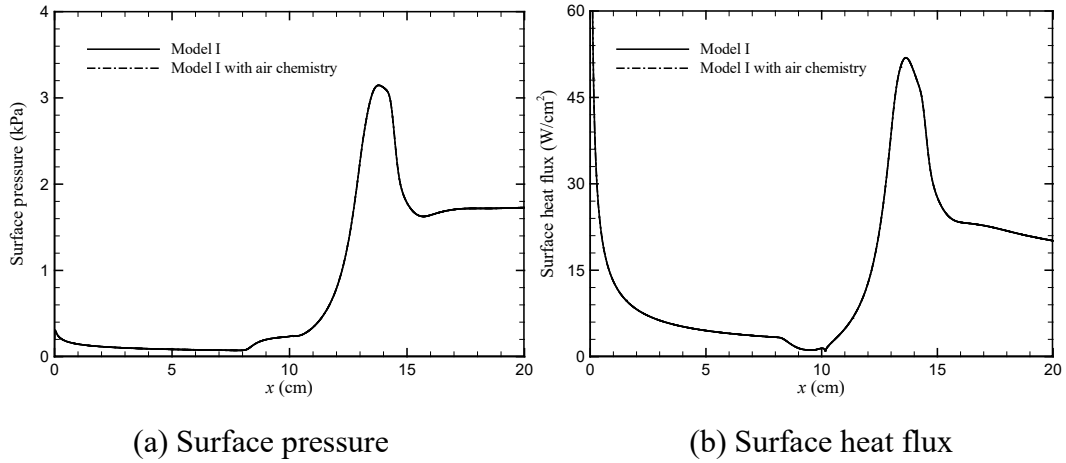and without chemical reactions for the double-cone configuration.

(a) Surface pressure

(b) Surface heat flux

Fig. 4. Distributions of surface pressure and heat flux predicted by models I with and without chemical reactions for the hollow-cylinder flare configuration.
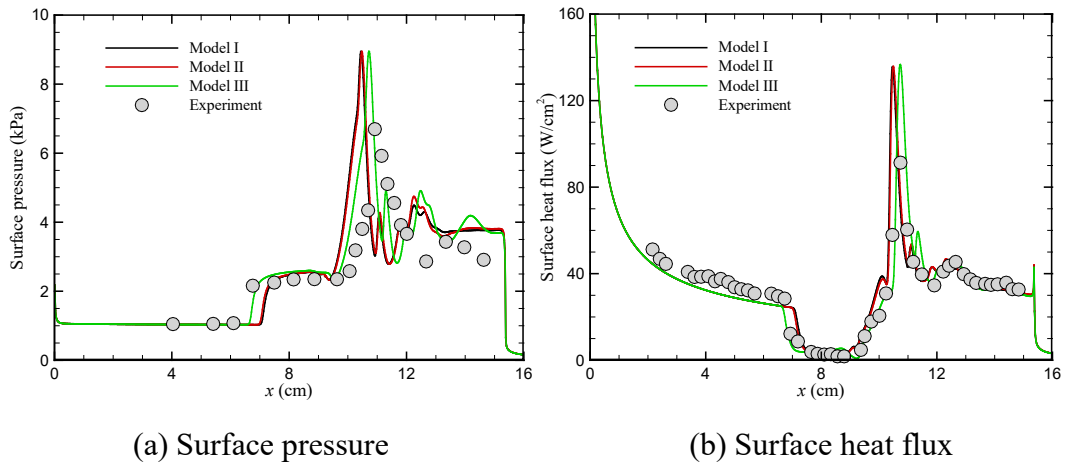

(a) Surface pressure

(b) Surface heat flux

Fig. 5. Distributions of surface pressure and heat flux predicted by different models for the double-cone configuration.

(a) Model I
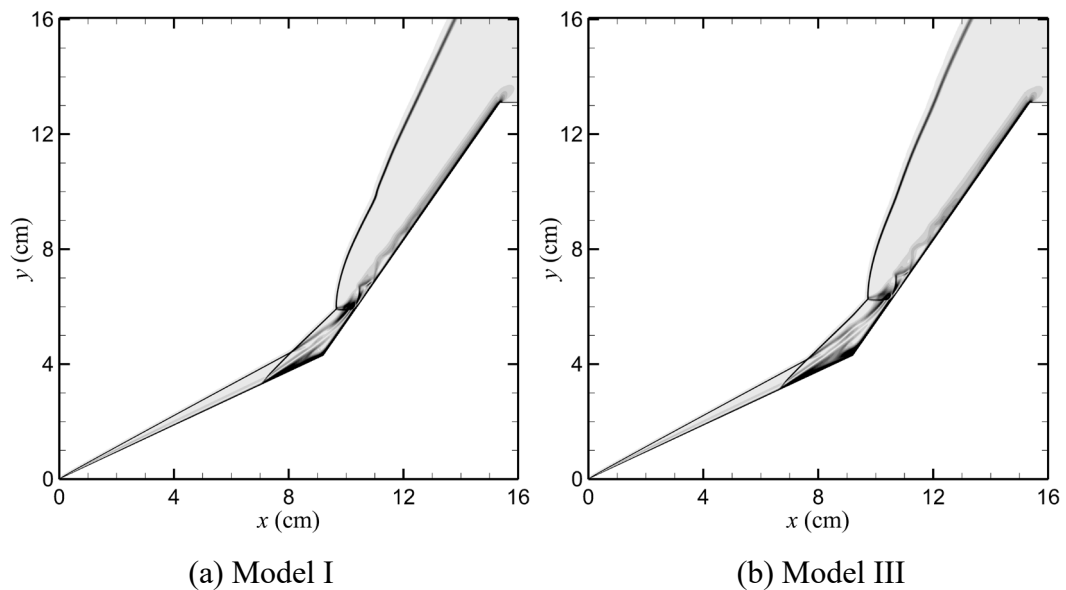
(b) Model III

Fig. 6. Contours of the density gradient magnitude predicted by models I and III

(a) Model I

(b) Model III

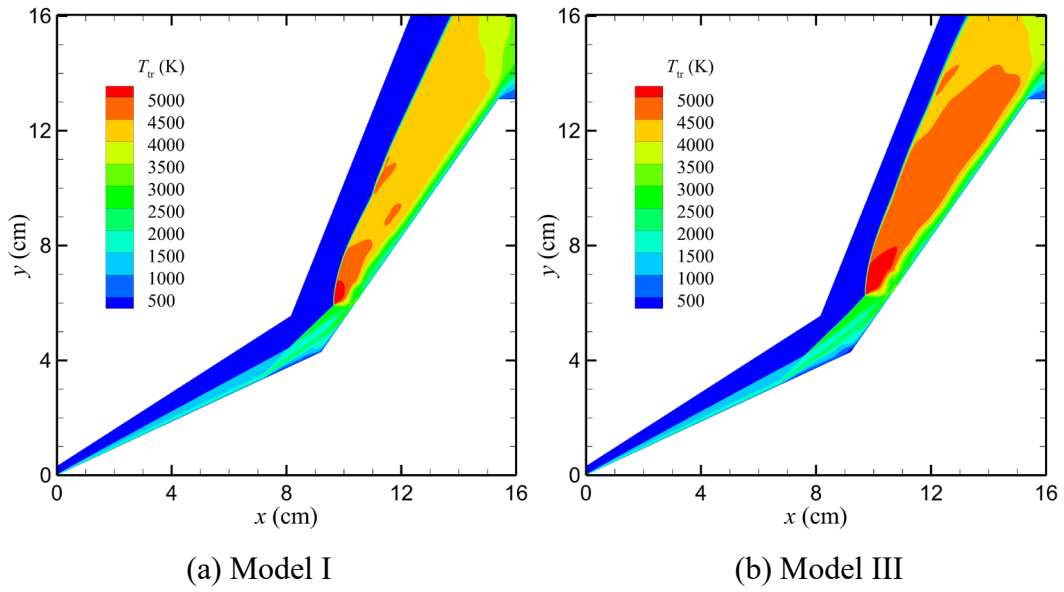**Fig. 7. Contours of the translational–rotational temperature predicted by models I and III for the double-cone configuration.**

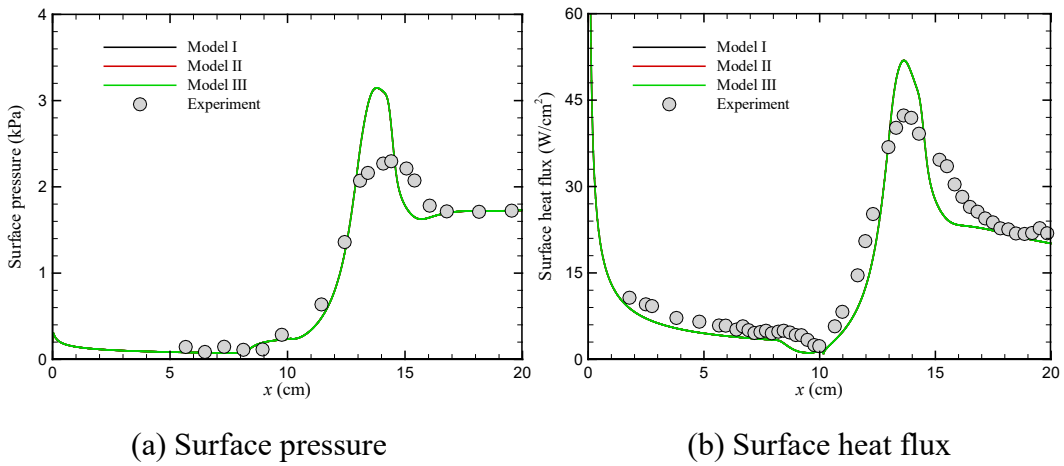(a) Surface pressure

(b) Surface heat flux

Fig. 8. Distributions of surface pressure and heat flux predicted by different models for the hollow-cylinder flare configuration.